

# A Nonlinear Adaptive Method for Microjet-Based Flow Separation Control

Brandon M. Reese\*, Farrukh S. Alvi†, and Emmanuel G. Collins Jr.‡

*Florida Center for Advanced Aero-Propulsion*

*Florida A&M University - Florida State University*

*Tallahassee, FL, 32310, USA*

For airborne air-breathing systems, flow separation is a critical factor in efficiency, ease of piloting, and performance capability. Flow separation, or stall, leads to increased drag, decreased lift, and unpredictable vibrations due to unsteadiness. Small aerial vehicle flight is one such application. On these systems, effective control of stall could provide greater maneuverability and performance, and lessened vibration during optical image capture. Separated flow is a macro-scale phenomenon and is governed by complex flow interactions but can be controlled by micro-scale actuation. For many decades, passive control methods such as vortex generators and surface roughness have been designed to mitigate separation under conditions of steady, design-point operation. Not until recently, however, has the emergence of closed loop methods enabled control of separation that is able to respond as flow conditions change. Advances in microprocessor technology have now enabled the use of sophisticated adaptive control methods that achieve separation control with linear time-varying models. While adaptive control methods have improved upon passive and open-loop techniques for steady operation, nonlinear adaptive control has yet to be demonstrated for the dynamic flow conditions of agile flight. Adaptive Sampling Based Model Predictive Control (Adaptive SBMPC), a novel approach to nonlinear Model Predictive Control, is presented. Adaptive SBMPC applies the Minimal Resource Allocation Network algorithm for nonlinear system identification and the Sampling Based Model Predictive Optimization algorithm to achieve effective feedback control of flow separation. By introducing a computationally efficient nonlinear approach to the adaptive control of separation, this research experimentally demonstrates real time control of flow separation for a range of flow conditions.

---

\*Graduate Research Assistant, Department of Mechanical Engineering, [bmr09f@my.fsu.edu](mailto:bmr09f@my.fsu.edu).

†Professor and FCAAP Director, Department of Mechanical Engineering, [alvi@eng.fsu.edu](mailto:alvi@eng.fsu.edu), Associate Fellow AIAA.

‡Professor and Chair, Department of Mechanical Engineering, [ecollins@eng.fsu.edu](mailto:ecollins@eng.fsu.edu).

## I. Introduction

For decades, flow separation has been of particular interest in engineering applications where improved aerodynamic performance is desired. Control of flow separation, both active and passive, is a key component of existing aviation technology. Passive control methods, such as leading edge surface roughness or the inclusion of vortex generators, rely on a stationary structural component to produce a reduction or delay in separation effects. These techniques typically produce an early transition to turbulence or streamwise vortical structures, each of which have been shown to mitigate separation.<sup>1</sup> The effectiveness of passive techniques is limited in comparison with active techniques, which rely on powered mechanisms to alter the flow, especially when conditions off the design point are considered.<sup>2</sup> These types of off-design conditions are common for aircraft that perform maneuvers, micro-aerial vehicles, and aeronautical systems that are deployed in diverse environments.

The significant increase in capability and decrease in cost of computing hardware has led to the feasibility of active control techniques of increasing sophistication. Both open-loop and closed-loop control schemes have been applied to flow control problems and there is evidence that closed loop approaches offer significant improvement in performance over open-loop control<sup>3,4</sup>.

Several areas of flow control research, including suppression of cavity flow resonant tones and mitigation of flow separation, have advanced rapidly in recent years as new technologies have both created demand for and expanded the capabilities of such systems. The study of cavity flow control has demonstrated that mathematical techniques such as Proper Orthogonal Decomposition (POD) and model reduction are effective tools for controlling aerodynamic systems<sup>5,6</sup>. While these studies incorporated flow visualization and analysis efforts to produce nonlinear models that are effective for developing open-loop control strategies, it has been more practical to linearize these models for the sake of computational efficiency when implementing real-time closed loop control<sup>3,4</sup>.

Frequency domain methods have been applied to model and control the flow dynamics in flow control and related applications<sup>7,8,9</sup>. Nonlinear POD methods similar to those applied to cavity flow have also been used for flow separation;<sup>10</sup> however, these models exhibit little robustness and have only been used to perform open-loop control. Actuator development has also been key to the recent advances in the field of flow separation control. Both synthetic jet unsteady actuators<sup>11,12</sup> and steady microjet actuators<sup>8,13</sup> have been effective in closed-loop separation control experiments. Because of the advantage of high momentum capability with low power requirements,<sup>14</sup> microjet arrays are used as actuators in research. The actuators described in this research are capable of both pulsed and steady blowing.

The control method presented in this paper is unique from past results because a nonlinear model is identified and used for closed-loop control. The method is implemented with experimental hardware and the identification and control processing is executed in real time.

The primary objective of this research is to maximize the lift coefficient  $C_L$  by means of delaying the onset of separation as well as controlling the already-separated boundary layer flow, but by common observation  $C_L/C_D$  is usually also improved when flow separation is mitigated to increase  $C_L$ . Given a discrete time series of multiple sensor measurements located along an airfoil's chord (inputs), the proposed research aims to determine an optimal series of microjet pressure signals (outputs), maximizing the lift-to-drag ratio of the airfoil. The control system should achieve this task for a broad range of steady or dynamically-prescribed Reynolds number or angle of attack parameters. This is to be accomplished without direct measurement of either parameter and without the modification of tuning parameters.

## II. Control Method

As a means of solving Model Predictive Optimization problems without computing gradients, Sampling Based Model Predictive Control (SBMPC) has been developed and implemented on experimental platforms<sup>15,16,17</sup>. SBMPC may be applied to solve the nonlinear optimization problem,

$$\min_{\{\mathbf{u}(k), \dots, \mathbf{u}(k+N-1)\}} \sum_{i=0}^{N-1} C(\mathbf{y}(k+i+1) - \mathbf{r}(k+i+1)) \quad (1)$$

where the cost function  $C(\bullet) \geq 0$ , subject to the nonlinear state space equations,

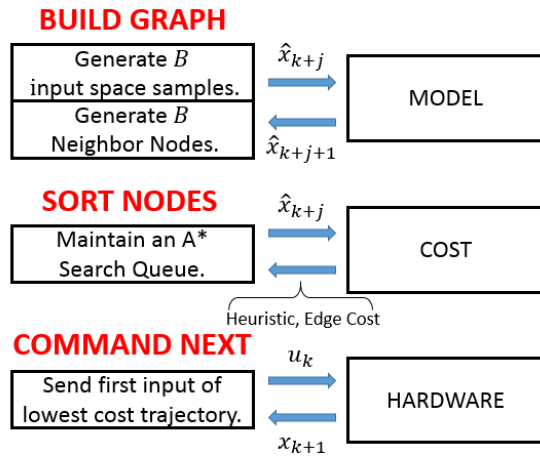


Figure 1. Sampling Based Model Predictive Control Summary. The algorithm discretizes the input space and makes model-based state predictions,  $\hat{x}_{k+j}$ , in order to minimize a cost function.

$$\mathbf{x}(k+i) = g(\mathbf{x}(k+i-1), \mathbf{u}(k+i-1)), \quad (2)$$

$$\mathbf{y}(k) = h(\mathbf{x}(k)), \quad (3)$$

and the constraints,

$$\mathbf{x}(k+i) \in \mathbf{X}_{free} \quad \forall \quad i \leq N, \quad (4)$$

$$\mathbf{u}(k+i) \in \mathbf{U}_{free} \quad \forall \quad i \leq N, \quad (5)$$

where  $r(k)$  is the reference input and  $\mathbf{X}_{free}$  and  $\mathbf{U}_{free}$  represent the states and inputs respectively that do not violate any of the problem constraints. SBMPC is described in Fig. 1 and is easily applied to both linear and nonlinear models, combining techniques for sampling the input domain with an efficient graph search method such as A\*.

## A. Sampling the Input Domain

The field of path planning in robotics has seen recent innovations that have used sampling techniques<sup>18, 19</sup>. SBMPC involves the sampling of the space of allowable inputs. Halton sampling, in particular, is a method based on the low-discrepancy Halton sequences that has been shown to provide representative sample sets consisting of fewer points than sets generated using pseudo-random numbers or regular grids<sup>20, 21</sup>. Satisfaction of input constraints is automatic, since it is the allowable inputs that are sampled, and since the inputs are propagated forward through the model, no inversion of the model is needed.

## B. The Graph Search

Using the current state and input samples, several nodes are computed by propagating the model and added to a graph with tree connectivity, as illustrated in Fig. 2. The branchout factor  $B$ , a tuning parameter of the algorithm, determines how many child nodes are generated when a particular parent node is expanded.

The Halton sequence algorithm, which is potentially used thousands of times at each time interval when the SBMPC routine is called, was a major contributor to the total runtime of SBMPC. Generating new Halton samples takes a median of 210 times longer than a lookup table query; therefore, precomputing these samples and storing them in memory enables the run-time code to execute much faster while yielding identical results. Note that although the uniform samples are generated offline, the transformation to a nonuniform distribution, described below, is not precomputed. In order to maintain integrity near the boundary of the input sampling domain, it is necessary to use a truncated, asymmetric distribution when sampling changes in an input that is near its boundary. Because this calculation is state-dependent, it is carried out in run-time which is a major contributor to the execution time difference between the cases of uniform and nonuniform sampling density.

The uniform sampling density typically used for SBMPC may be transformed in order to achieve greater

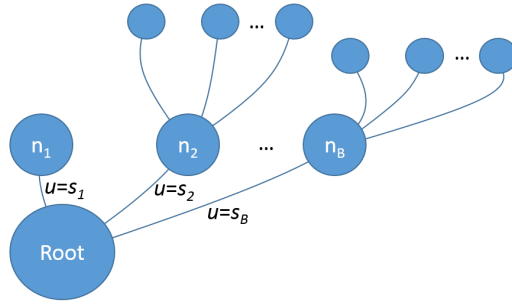


**Figure 2. SBMPC Search Graph.** The graph is built by expanding the most promising node to generate  $B$  child nodes. Each child node is assigned an input sample, which is propagated forward through the model to predict a state for that node. The potential cost of reaching that state is used to prioritize the nodes and select the most promising candidate for the next iteration of expansion.

relative sampling density in a desired region of the input domain. In order to preserve input constraint satisfaction, the range which was sampled by the uniform distribution should be maintained. The following procedure can be followed to obtain a nonuniform sampling distribution aggregated about zero:

1. Transform the samples to occupy the range  $[-1, 1]$  via affine transformation
2. Record the sign of each transformed sample
3. Raise each transformed sample to an integer power
4. Restore the sign (if even power) and apply the inverse transform to the samples

Using a nonuniform sampling density can improve the performance of SBMPC by reducing the branchout factor required to converge to some near-optimal trajectory.

### C. Nonlinear Modelling

Previous adaptive flow separation research has aimed to capture the nonlinear dynamics of the flowfield by identifying an instantaneously linearized model that varies with time. The optimization of a linear model has the advantages of speed and simplicity over those that consider nonlinear models. The unmodelled dynamics, however, can cause such techniques to be suboptimal and even unstable.

#### 1. Nonlinear POD Methods

Proper Orthogonal Decomposition (POD) techniques have been used to identify models in the form of polynomial difference equations<sup>22,23</sup> that are sufficient for open loop control design.<sup>5</sup> However, due to computational expense, closed loop flow control implementations have been limited to linear models. The primary advantage of SBMPO over alternative methods is that the optimization phase does not prefer linear to nonlinear models, and the algorithm does not need to compute closed-form gradients. Although SBMPO has the ability to optimize inputs to a POD model, POD models are steady state in nature and do not capture the transient behavior or hysteresis effects that are necessary to control dynamic stall.

#### 2. Nonlinear Neural Network Methods

The use of an artificial neural network allows nonlinear models to be identified in a general manner by composing a function that computes future outputs based on past states. For this application the state vector,

$$\mathbf{x}_k = (\mathbf{y}_{k-1}^T, \mathbf{y}_{k-2}^T, \dots, \mathbf{y}_{k-n_y}^T, \mathbf{u}_{k-1}^T, \mathbf{u}_{k-2}^T, \dots, \mathbf{u}_{k-n_u}^T)^T, \quad (6)$$

consists of  $n_u$  prior plant inputs and  $n_y$  outputs. The form,

$$\mathbf{y}_k = f(\mathbf{y}_{k-1}, \mathbf{y}_{k-2}, \dots, \mathbf{y}_{k-n_y}, \mathbf{u}_{k-1}, \mathbf{u}_{k-2}, \dots, \mathbf{u}_{k-n_u}) \equiv F(\mathbf{x}_k), \quad (7)$$

is known as as a nonlinear autoregressive exogenous inputs (NARX) model form because it is analogous to the autoregressive exogenous inputs (ARX) form for linear models. If  $F(\mathbf{x}_k)$  were a linear function, the equation would simplify to an ARX formulation,

$$\hat{\mathbf{y}}_k = A\mathbf{x}_k, \quad (8)$$

with the matrix  $A$  of constant coefficients.

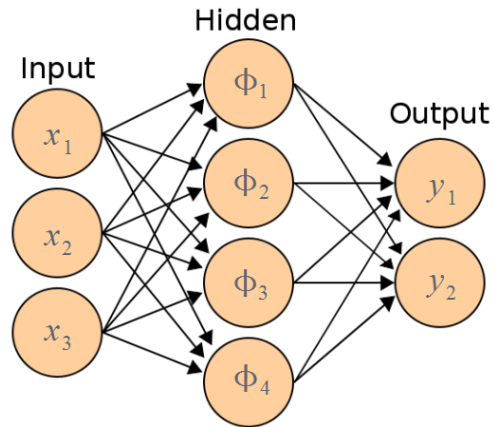


**Figure 3.** The layout of a sample RBF network consists of a hidden layer containing one hidden neuron for each distinct state pattern that the algorithm encounters. Collectively these pattern state vectors make up a basis with which all system dynamics are modelled. With enough of these hidden neurons the network is able to match arbitrarily complex nonlinear behavior.

While there are many ways to construct the nonlinear function  $F(\mathbf{x}_k)$ , neural network methods construct this function as a composition of simpler functions called neural units, which can be arranged in series and parallel to form a network. The network implemented in this research has a two-layer structure first proposed by Platt.<sup>24</sup> This Resource Allocation Network (RAN) has for its first layer, a collection of neural units that respond in parallel when state  $\mathbf{x}_k$  is nearby (according to the *Euclidean norm*) to a previously seen pattern. The Gaussian function is selected for the first layer to achieve this behavior in a simple computation with closed-form derivatives. The second layer combines these Gaussian outputs in a weighted sum, yielding the Radial Basis Function (RBF) representation,

$$F(\mathbf{x}_k) = \mathbf{a}_0 + \sum_{i=1}^N \mathbf{a}_i \phi_i, \quad (9)$$

$$\phi_i = \exp\left(-\frac{\|\mathbf{x}_k - \boldsymbol{\mu}_i\|^2}{\sigma_i^2}\right). \quad (10)$$

For each of the  $N$  neural units, the RAN algorithm must specify a basis vector  $\boldsymbol{\mu}_i$ , a Gaussian width  $\sigma_i$ , and weight coefficients  $\mathbf{a}_i$ . For a MIMO plant with  $m$  output signals and  $r$  input signals, the dimensionality of  $\mathbf{x}_k$  and  $\boldsymbol{\mu}_i$  is  $(n_y m + n_u r) \times 1$ , and  $\mathbf{a}_i$  is  $n_y \times 1$ . As illustrated in Fig. 3, the RBF network uses a summation of Gaussian elements to approximate the nonlinear mapping from the input space to the output space.

When online identification begins, the RAN network has no hidden units ( $N = 0$ ). At each timestep, the algorithm will either grow the network by adding a hidden unit, or refine all current parameters by performing an Extended Kalman Filter (EKF) update. A hidden unit is added when the error heuristics are large, and the EKF update is performed when the error heuristic is small.<sup>25</sup> The tuning of the error heuristic is important because this will determine how quickly the network grows. The heuristic condition for the addition of a new hidden unit is threefold, requiring simultaneous satisfaction of

$$\|\mathbf{e}_k\| = \|\mathbf{y}_k - \hat{\mathbf{y}}_k\| > E_1, \quad (11)$$

$$e_{rms,k} = \sqrt{\sum_{j=k-(M-1)}^k \frac{\|\mathbf{e}_j\|^2}{M}} > E_2, \quad (12)$$

and

$$d_k = \|\mathbf{x}_k - \boldsymbol{\mu}^*\| > E_3. \quad (13)$$

The instantaneous error inequality (11) requires the current prediction error  $\mathbf{e}_k$  to be greater than threshold  $E_1$ , the cumulative error inequality (12) requires RMS error over the past  $M$  timesteps to be greater than threshold  $E_2$ , and the centroid spacing inequality (13) requires the distance between the state vector and the nearest existing hidden unit centroid vector  $\boldsymbol{\mu}^*$  to be greater than  $E_3$ .

In any timestep where all three conditions are met, a new hidden unit is introduced with parameters valued to cancel out the instantaneous error:

$$\mathbf{a}_{N+1} = \mathbf{e}_k, \quad \boldsymbol{\mu}_{N+1} = \mathbf{x}_k, \quad \sigma_{N+1} = \kappa \|\mathbf{x}_k - \boldsymbol{\mu}^*\|, \quad (14)$$

where the initial Gaussian width  $\sigma_{N+1}$  depends on basis function overlap parameter  $\kappa$ .

In any timestep where a hidden unit was not introduced, the EKF update is performed on the vector of all data-based parameters

$$\mathbf{w} = [\mathbf{a}_0^T, \mathbf{a}_1^T, \boldsymbol{\mu}_1^T, \sigma_1, \dots, \mathbf{a}_N^T, \boldsymbol{\mu}_N^T, \sigma_N]^T. \quad (15)$$

It is necessary to compute the gradient matrix  $\mathbf{B}_k \equiv \nabla_{\mathbf{w}} F(\mathbf{x}_k)$  for the current timestep, which is evaluated as

$$\mathbf{B}_k = [\mathbf{I}_{n_y}, \phi_1 \mathbf{I}_{n_y}, \phi_1 (2\mathbf{a}_1 / \sigma_1^2) (\mathbf{x}_k - \boldsymbol{\mu}_1)^T, \phi_1 (2\mathbf{a}_1 / \sigma_1^3) \|\mathbf{x}_k - \boldsymbol{\mu}_1\|^2, \dots, \phi_N \mathbf{I}_{n_y}, \phi_N (2\mathbf{a}_N / \sigma_N^2) (\mathbf{x}_k - \boldsymbol{\mu}_N)^T, \phi_N (2\mathbf{a}_N / \sigma_N^3) \|\mathbf{x}_k - \boldsymbol{\mu}_N\|^2]^T, \quad (16)$$

where  $\mathbf{I}_{n_y}$  is the  $n_y \times n_y$  identity matrix, and  $\phi_i$  is the Gaussian function of Eq. (10) evaluated in the  $i^{\text{th}}$  hidden unit. To perform the EKF update, define the Kalman gain matrix

$$\mathbf{K}_k = \mathbf{P}_{k-1} \mathbf{B}_k [\mathbf{R}_k + \mathbf{B}_k^T \mathbf{P}_{k-1} \mathbf{B}_k]^{-1}, \quad (17)$$

with system error covariance and sensor noise covariance matrices  $\mathbf{P}$  and  $\mathbf{R}$ . In the RAN algorithm,  $\mathbf{R}$  is constant and is specified by sensor properties or offline measurements. Each EKF step,  $\mathbf{P}$  is updated by

$$\mathbf{P}_k = [\mathbf{I}_{n_w} - \mathbf{K}_k \mathbf{B}_k^T] \mathbf{P}_{k-1} + q \mathbf{I}_{n_w}, \quad (18)$$

where  $q$  is a step size parameter and dimension  $n_w$  is the number of elements in  $\mathbf{w}$ . The parameters are updated to reduce the size of the identification error

$$\mathbf{w}_k = \mathbf{w}_{k-1} + \mathbf{K}_k \mathbf{e}_k. \quad (19)$$

On timesteps in which a hidden unit was introduced, the dimensionality of  $\mathbf{P}$  must increase by the number  $n_1$  of parameters that are added to  $\mathbf{w}$ , yielding

$$\mathbf{P}_k = \begin{pmatrix} \mathbf{P}_{k-1} & 0 \\ 0 & \gamma_0 \mathbf{I}_{n_1} \end{pmatrix}. \quad (20)$$

The parameter  $\gamma_0$  is an initial estimate of the variance for newly assigned data-based parameter values. This cycle of either network growth or EKF updates repeats until terminated. The RAN algorithm combines EKF gradient based optimization with heuristic based pattern recognition and learning to produce identified models that approximate general nonlinear dynamics in an efficient manner. A pruning step is added to the RAN algorithm by Yingwei et al. to produce the Minimal Resource Allocation Network (MRAN) algorithm.<sup>26</sup> This step removes hidden units whose relative contribution to the overall network output falls below a threshold for a number of consecutive time steps. The pruning threshold and window size, along with the network growth parameters  $E_1$ ,  $E_2$ , and  $E_3$  are chosen empirically to maintain the desired network size and convergence rate. The steps of the MRAN identification algorithm are summarized by Fig. 4.

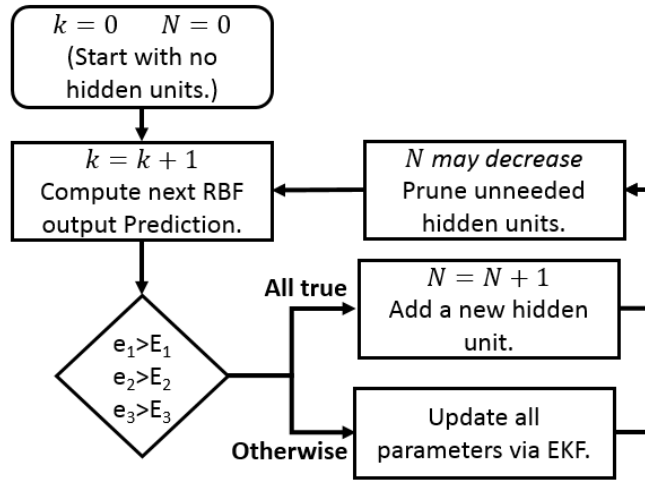


Figure 4. The basic MRAN algorithm combines heuristically driven construction of an RBF network with automatic parameter tuning using an EKF.

### III. Results

Results are presented for wind tunnel experiments with the goal of mitigating separation and therefore controlling lift. This section contains a description of the experimental setup in Subsection A, results of open-loop characterization tests in Subsection B and results of closed-loop control in Subsection C.

#### A. Flow Control Experimental Setup

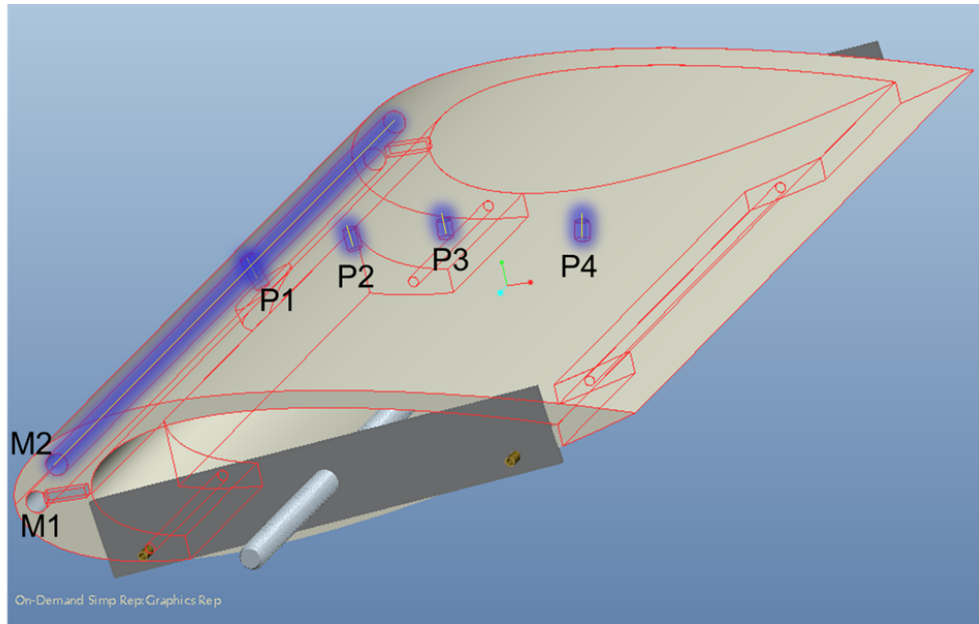


Figure 5. Airfoil Schematic. This diagram includes microjet array and pressure transducer locations. The pressure transducers at four distinct locations gives enough information about the surface pressure distribution to approximate lift. The same airfoil design is used in simulation and experiments.

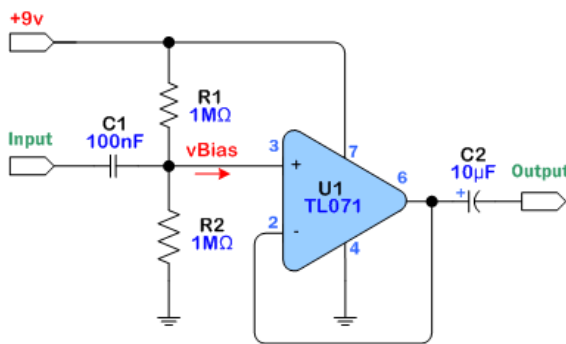
The wind tunnel experiments were carried out in the subsonic closed return wind tunnel at the FAMU-FSU College of Engineering. This wind tunnel has a 12" x 12" square test section and is capable of operation

between 3.5 m/s and 35 m/s. The NACA 0025 airfoil model of Fig. 5 is used in the following tests and is mounted to allow a variable pitch angle. Sensor and actuator placement is given in Table 1. At each pressure transducer location, P1 through P4, an Endevco unsteady pressure transducer (1 psi range) was mounted flush with the airfoil surface along the center chord. At each microjet location, M1 and M2, an array of 40 equally-spaced microjets were drilled into the channel, normal to the airfoil surface. Each microjet channel was supplied from both ends by plastic tubing to the output end of a solenoid valve (SensorTechnics HF Pro). The input end of the solenoid valve was attached to a steady pressure source supply between 0.5 psi and 10 psi. In each experiment, angle of attack was measured by taking a side view photograph and comparing pixel coordinates of the support pins to pixel coordinates of points on the tunnel wall.

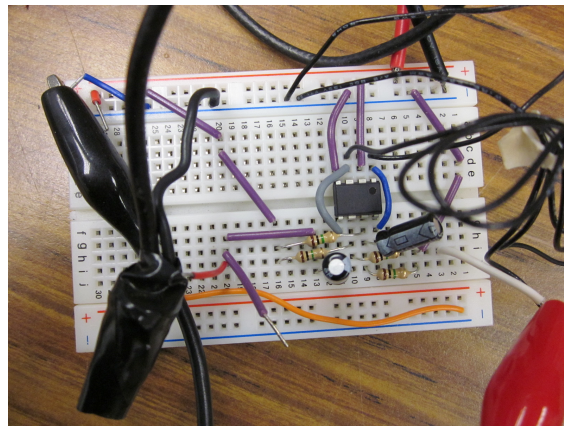
**Table 1. Chord Locations of Microjets and Transducers.**

Component	M1	M2	P1	P2	P3	P4
$x/c$	0.0	0.063	0.127	0.300	0.452	0.667

During tests, data signals from the four pressure transducers were amplified using a Kendrick & Associates multichannel amplifier and acquired digitally using dSPACE hardware. The command signals to pressure transducers were sent from dSPACE and amplified using the op-amp buffer circuit of Fig. 6. In open and closed loop testing, the single-input cases used only microjet array M2, and the two-input cases used both arrays M1 and M2, supplied independently by two solenoid valves.



(a) Circuit Diagram for Voltage Buffer.



(b) Two Buffer Circuits Breadboard Layout Using a Dual Channel Op Amp.

**Figure 6. Buffer Circuit Diagram and Photograph.**

## B. Open-Loop Characterization

Open loop characterization of the flow separation control system consisted of frequency sweep command. The supply voltage was a 50% duty cycle square wave of increasing frequency. After making pressure measurements for a steady supply pressure, the frequency was increased from 0 Hz to 300 Hz in 6 Hz increments, and 3 seconds of data was taken at each frequency. Measurements consisted of signals from pressure transducers located at the microjet channel (at the edge of the airfoil span) and at the microjet exit (2mm from the jet exit at the center of the airfoil span). The results of one case of these tests, performed on a bench top setup, are shown in Fig. B.

The data was sampled at 2 kHz, and time and frequency domain analysis is to be carried out on these measurements. From 0 to approximately 80 Hz, the pressure output frequency is identical to the voltage excitation frequency. Above 80 Hz, mode switching occurs due to the dynamics of the solenoid valve. The valve, which is designed for 30 Hz operation, switches primarily between the input frequency and  $\frac{1}{2}$  of the input frequency.

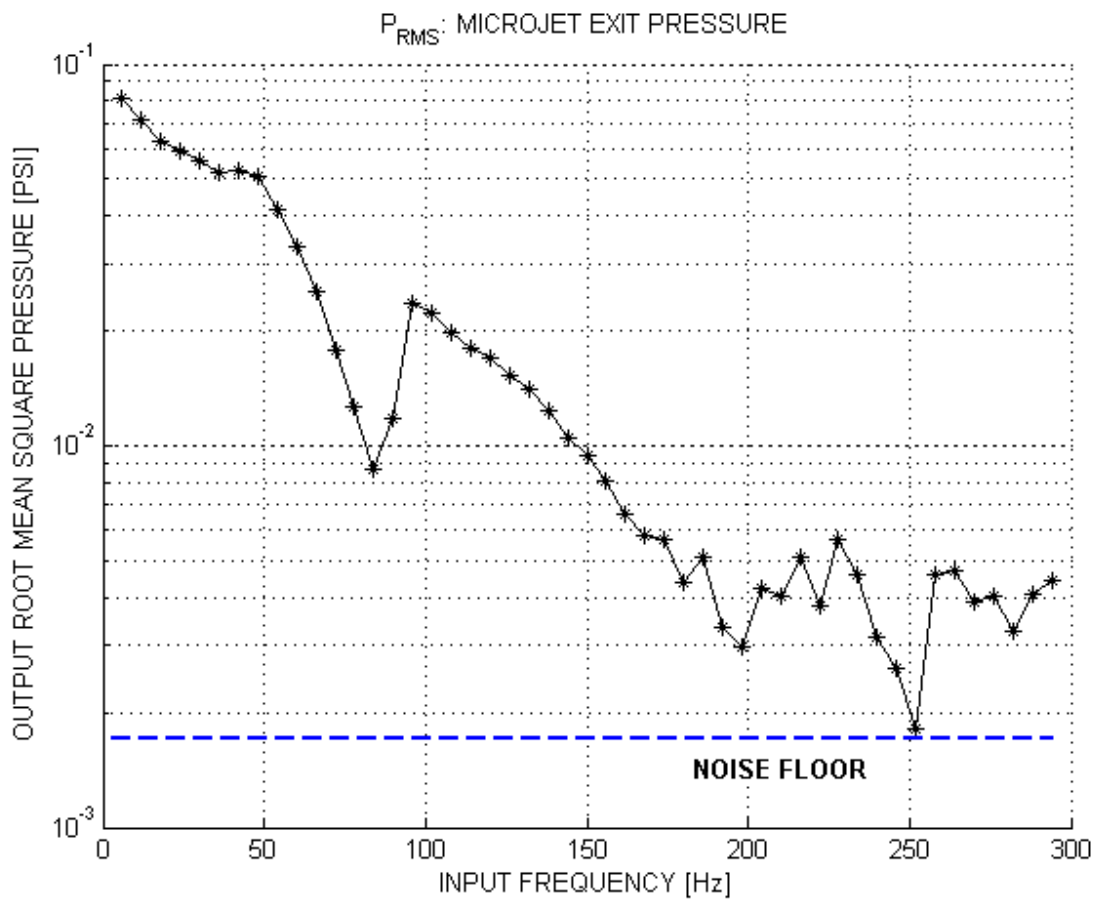


Figure 7. Open Loop  $P_{rms}$  at the Microjet Exit.

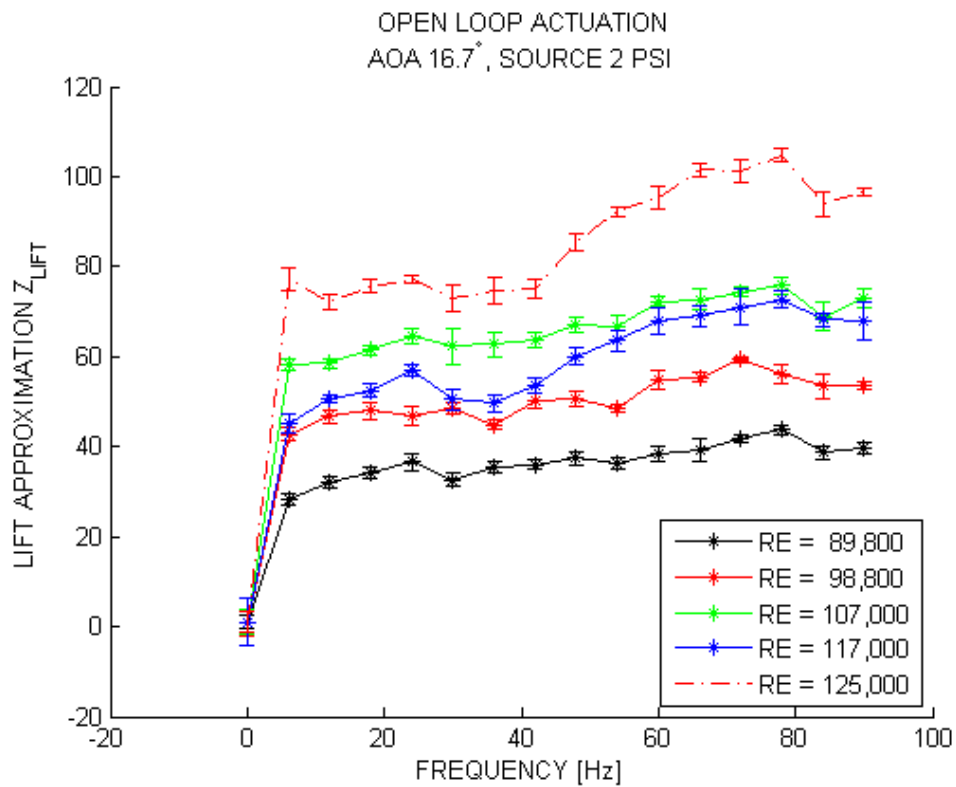


Figure 8.  $Z_{lift}$  response to frequency actuation at AOA = 16.7°.

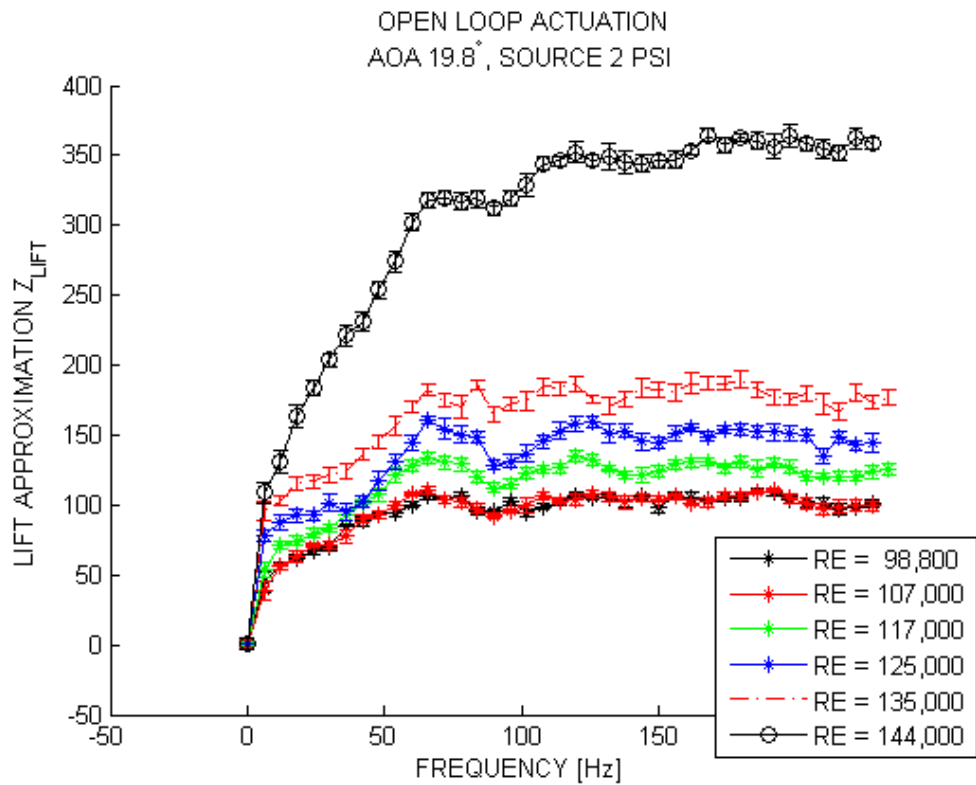


Figure 9.  $Z_{lift}$  response to frequency actuation at AOA = 19.8°.

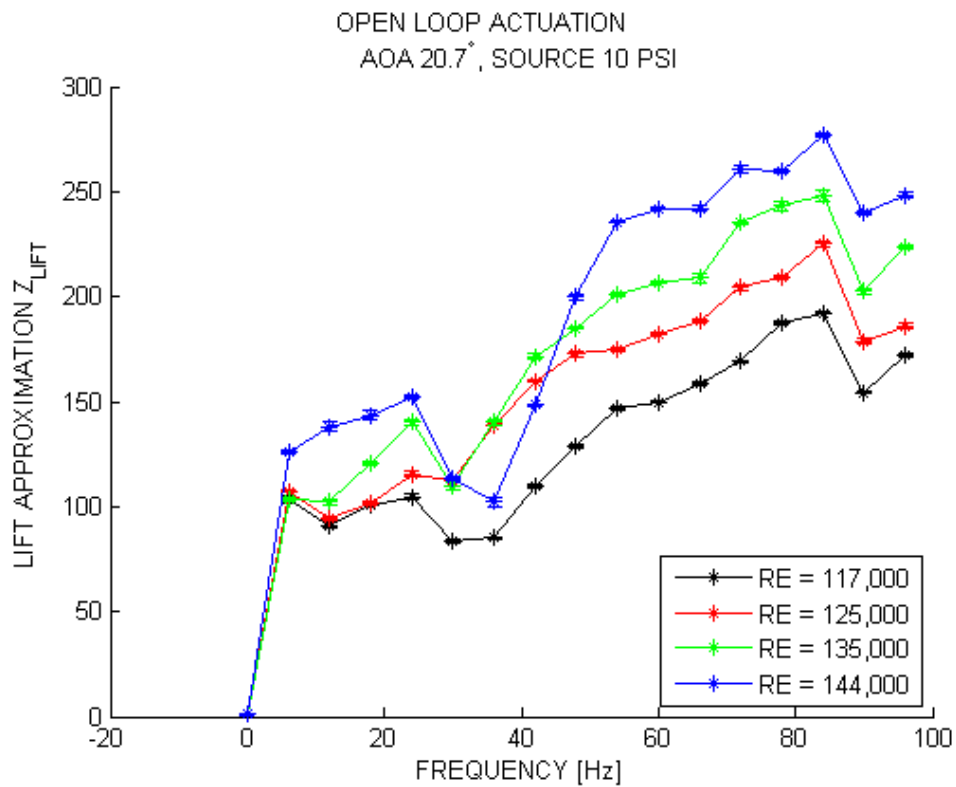


Figure 10.  $Z_{lift}$  response to frequency actuation at AOA = 20.7°.

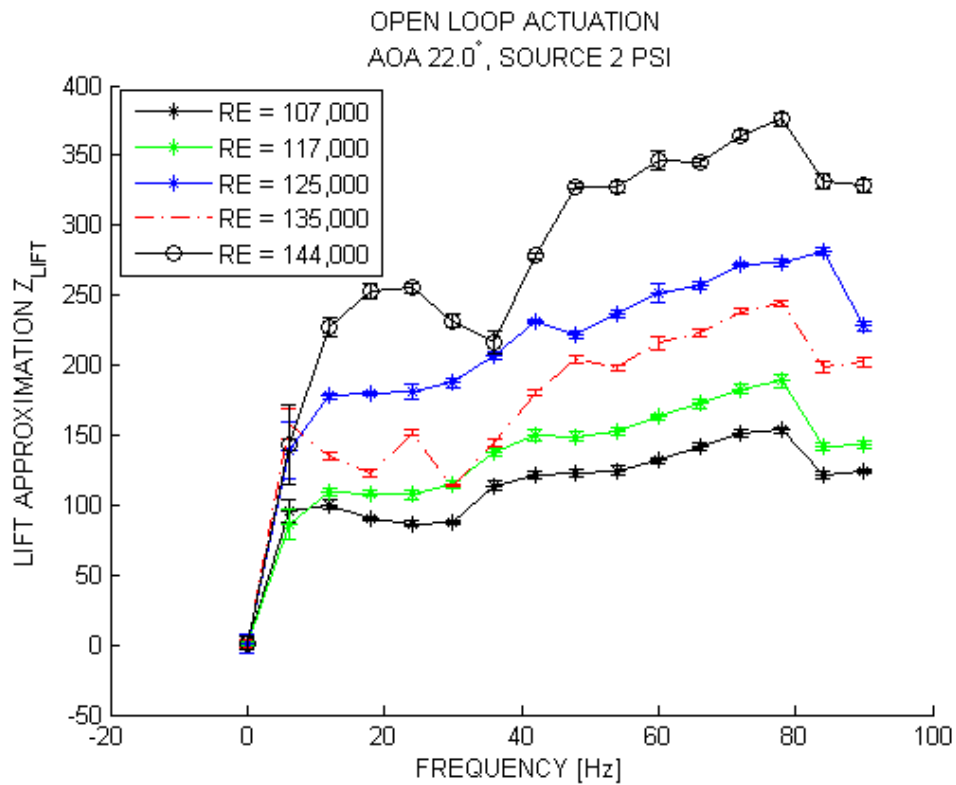


Figure 11.  $Z_{lift}$  response to frequency actuation at AOA = 22.0°.

Microjet exit pressure data is plotted in Fig. B. In order to attain reasonable SNR at the jet exit, the source pressure was increased to 10 psi. Compared to the microjet channel measurements, similar trends were observed in magnitude and frequency of pressure measurements at the microjet exit.

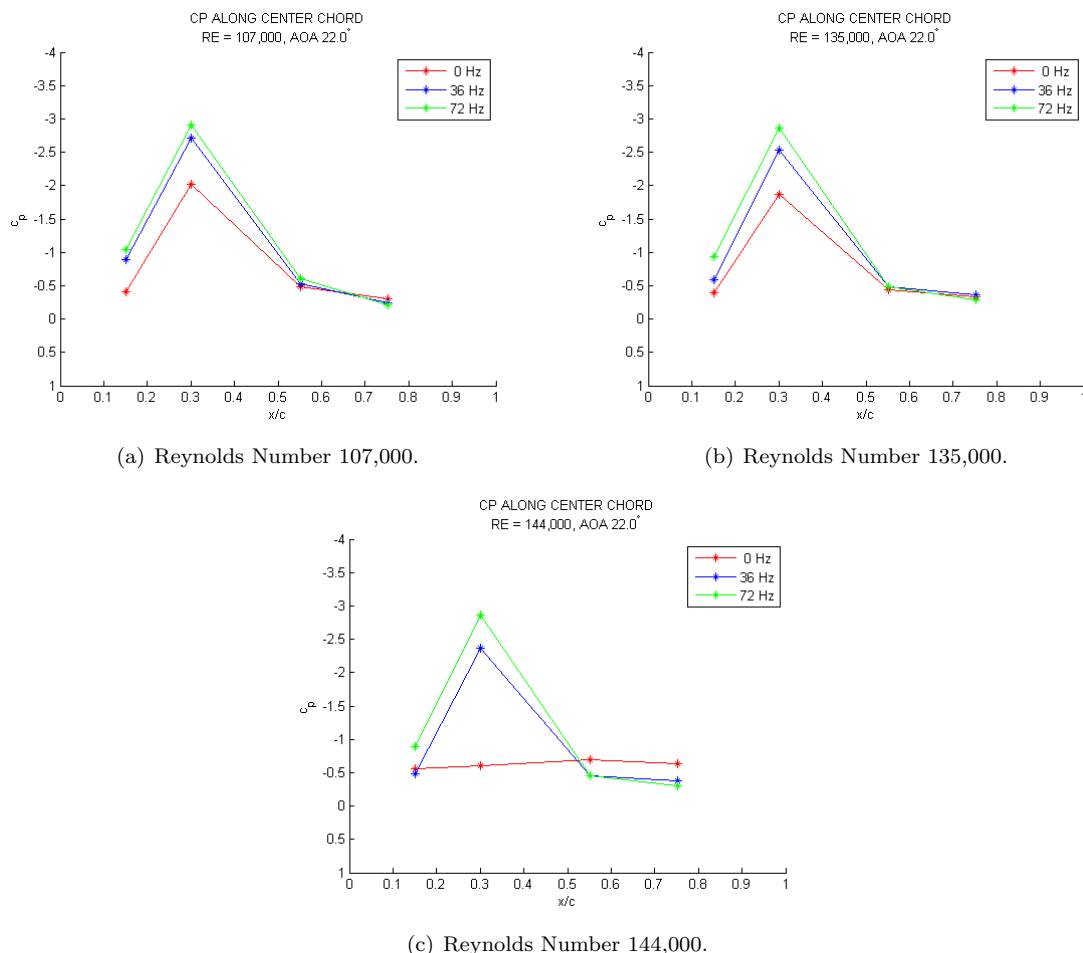


Figure 12. Measured  $c_p$  Values at Pressure Transducer Locations.

In addition to bench top characterization, the open loop response of the overall system was measured in the wind tunnel. The input for these tests was solenoid valve voltage frequency, and the output was  $Z_{lift}$ , the lift based performance function computed from the transducer measurements at locations P1 through P4. Changes in command voltage frequency were observed to cause changes in the steady state value of  $Z_{lift}$ . After each 6 Hz frequency increment, data was collected after the system reached a steady state. The data is presented in Figs. 8, 9, 10, and 11. Evidence of an actual change in lift as  $Z_{lift}$  changes is given in the  $c_p$  plots of Fig. 12. These discrete  $c_p$  measurements suggest that the magnitude of the area under the curve increases when going from 0 Hz to 72 Hz, which corresponds to greater suction on the upper surface and higher lift. Further evidence includes observations of flow attachment indicated by alignment of tufts on the airfoil surface as well as strong moments that were able to rotate the airfoil setup when the microjets were actuated without the shaft clamped in place.

### C. Closed-Loop Control

Frequency sweeps as mentioned above were used to train the neural network and represent the input-output behavior of the system with a nonlinear model. Using a model initialized with sweep data, Adaptive SBMPO was applied to perform closed loop control. During the test phase, the identification algorithm was enabled, but the control algorithm was disabled. During the control phase, the controller was enabled and could successfully track the desired reference value of  $Z_{lift}$ . In these plots, the Lift Performance Function is

$Z_{lift}$  normalized (divided by 100) to match the order of magnitude of the input space in order to simplify the Neural Network. Reference tracking capability is demonstrated in Figs. 13 through 18 for a variety of reference trajectories. Figs. 19 and 20 show the control adjustment in reaction of the control system to changes in Reynolds Number. The system adjusts the neural network model at the same time as the updated control signal is being computed and executed.

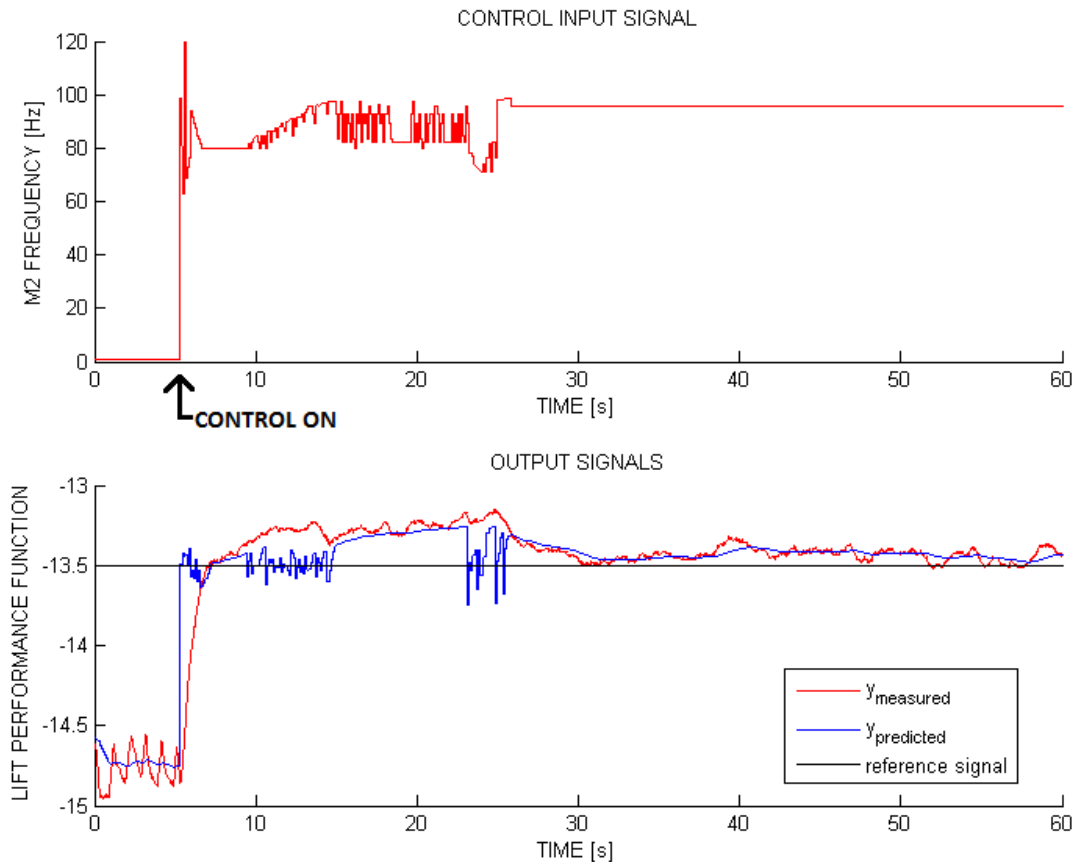


Figure 13. Closed Loop Case 1. The Reynolds number is 125,000, and the angle of attack is  $20^\circ$ .

## IV. Conclusions and Future Work

Closed loop control of separated flows has been demonstrated using the Adaptive SBMPC control system. To date, only a few selected cases have been run. Future tests will cover a wide range of flow conditions and will also incorporate Multiple Input Multiple Output control by enabling both rows of microjets, M1 and M2. Further analysis and flow visualization tests will quantify the achieved lift gains and provide insight into the control authority of the microjet actuators and cost-benefit balance of the overall control system.

## References

- <sup>1</sup>Kumar, V., *Separation Control in Adverse Pressure Gradient using High-Speed Microjets*, Phd dissertation, Mechanical Engineering, Florida State University, Tallahassee, FL, 2008.
- <sup>2</sup>Cattafesta, L., Tian, Y., and Mittal, R., "Adaptive Control of Post-Stall Separated Flow Application to Heavy Vehicles," *Springer Berlin Heidelberg Lecture Notes in Applied and Computational Mechanics*, Vol. 41, No. 5, 2009, pp. 151–160.
- <sup>3</sup>P. Yan, M. Debiasi, X. Y. J. L. H. O. M. S., "Experimental Study of Linear Closed-loop Control of Subsonic Cavity Flow," *AIAA*, Vol. 44, No. 5, 2006, pp. 929–938.

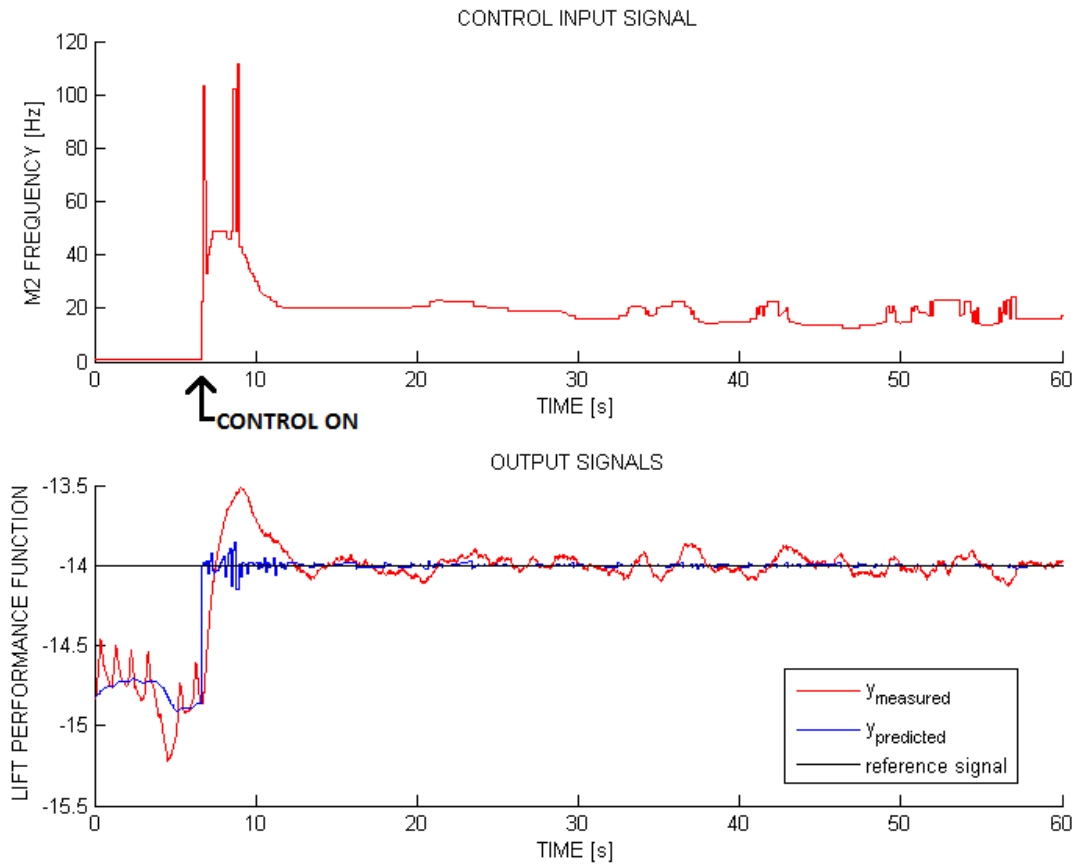


Figure 14. Closed Loop Case 2. The Reynolds number is 125,000, and the angle of attack is 20°.

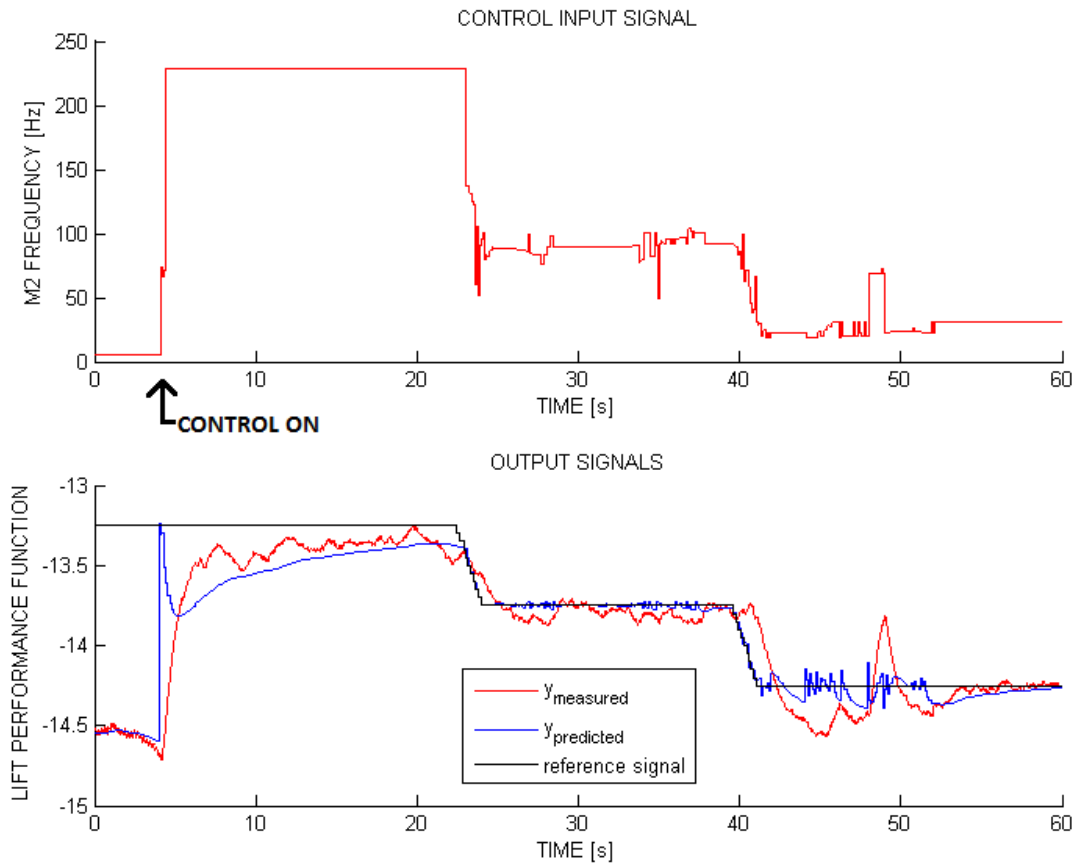


Figure 15. Closed Loop Case 3. The Reynolds number is 125,000, and the angle of attack is 20°.

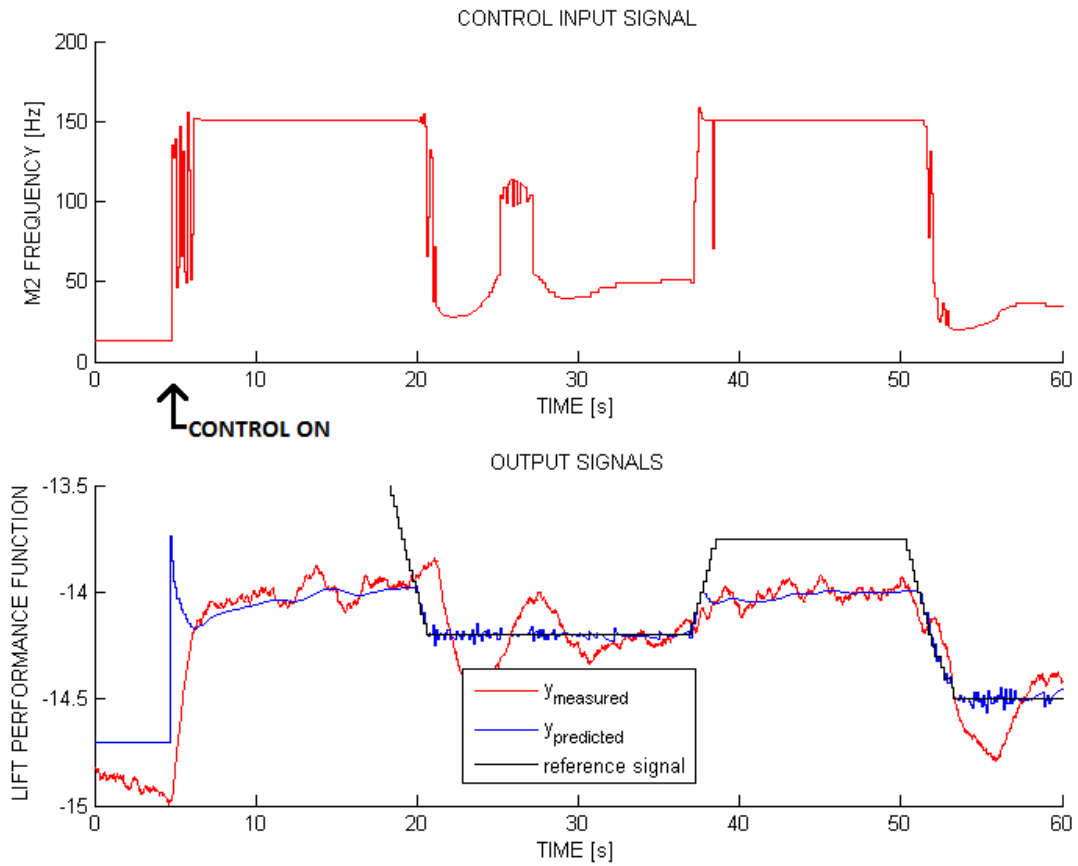


Figure 16. Closed Loop Case 4. The Reynolds number is 125,000, and the angle of attack is 20°.

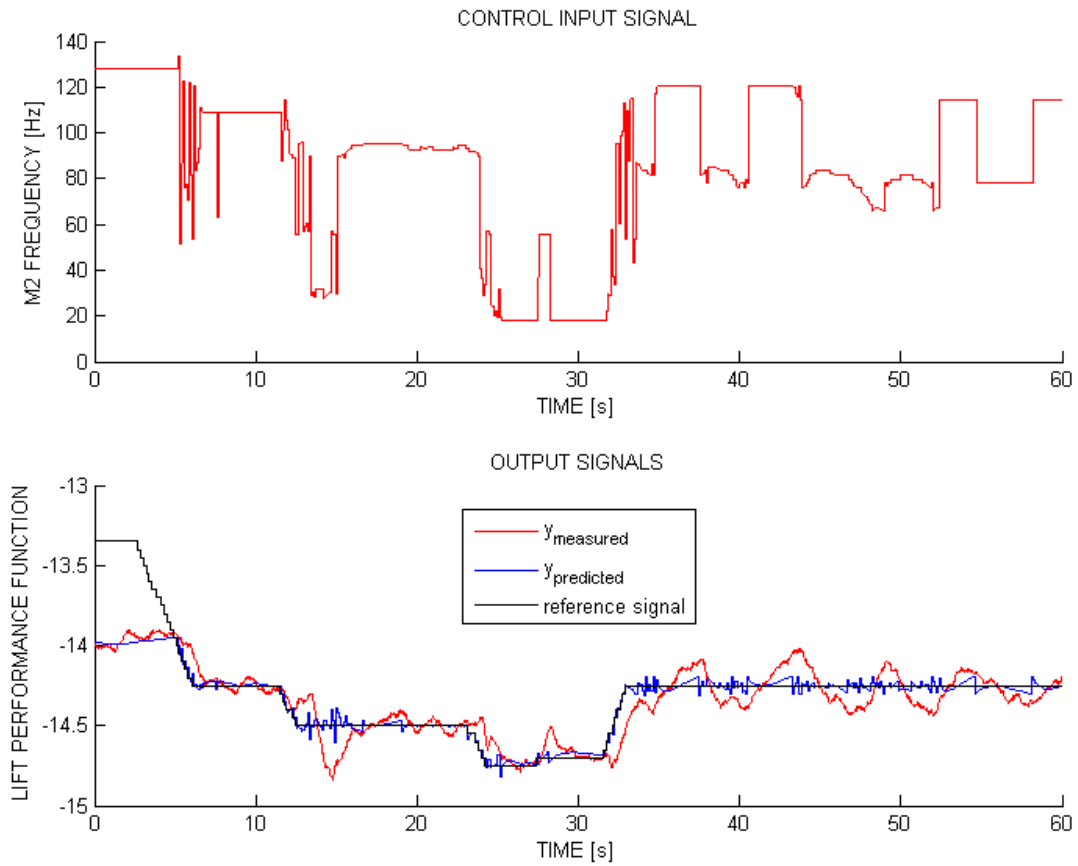


Figure 17. Closed Loop Case 5. The Reynolds number is 125,000, and the angle of attack is 20°.

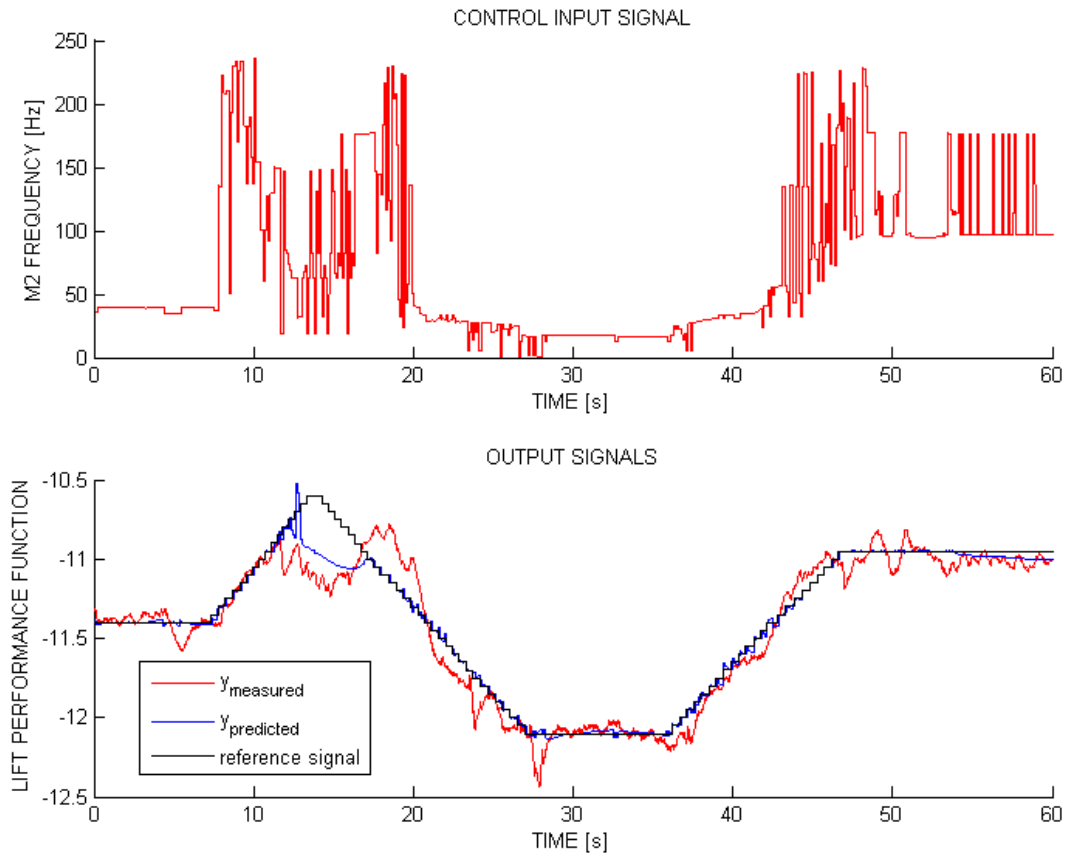


Figure 18. Closed Loop Case 6. The Reynolds number is 150,000, and the angle of attack is 20°.

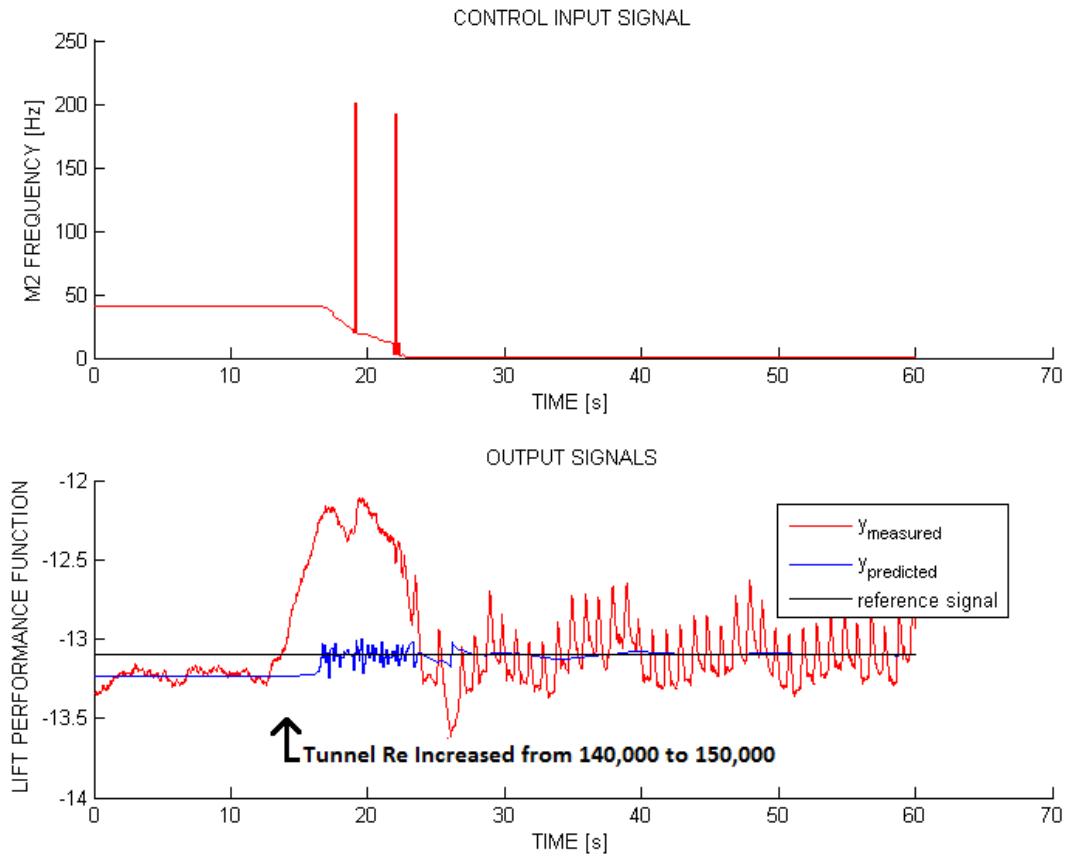


Figure 19. Closed Loop Case 6. The Reynolds number shifts from 140,000 to 150,000, and the angle of attack is  $20^\circ$ .

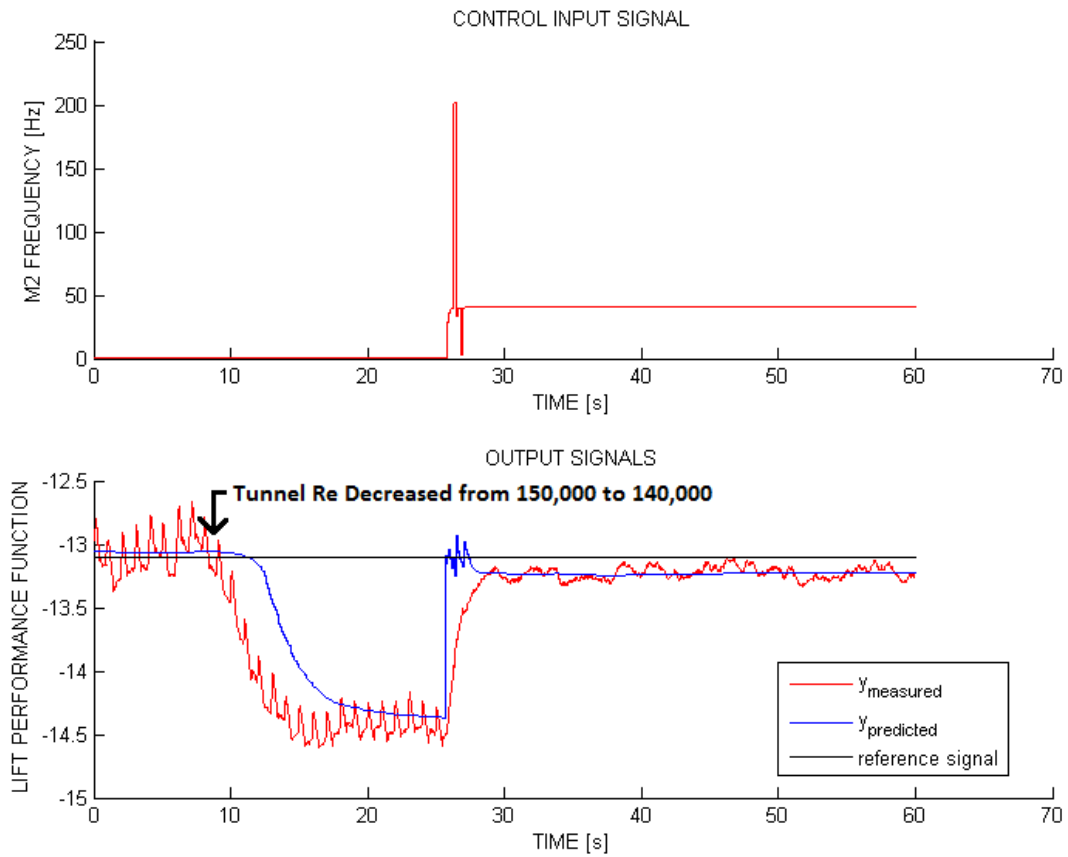


Figure 20. Closed Loop Case 6. The Reynolds number shifts from 150,000 to 140,000, and the angle of attack is  $20^\circ$ .

- <sup>4</sup>J. Little, M. Debiasi, E. C. M. S., “Effects of Open-loop and Closed-loop Control on Subsonic Cavity Flows,” *Physics of Fluids*, Vol. 19, No. 065104, 2007.
- <sup>5</sup>M. Samimy, M. Debiasi, E. C. A. S. X. Y. J. L. J. M., “Feedback Control of Subsonic Cavity Flows Using Reduced-order Models,” *Journal of Fluid Mechanics*, Vol. 579, 2007, pp. 315–346.
- <sup>6</sup>E. Caraballo, J. Little, M. D. M. S., “Development and Implementation of an Experimental Based Reduced-order Model for Feedback Control of Subsonic Cavity Flows,” *Journal of Fluids Engineering*, Vol. 129, No. 7, 2007, pp. 813–824.
- <sup>7</sup>M. Debiasi, J. Little, M. S., “Analysis of the Spectral Relationships of Cavity Tones in Subsonic Resonant Cavity Flows,” *Physics of Fluids*, Vol. 21, No. 055103, 2009.
- <sup>8</sup>Chuy, O. Y., Kumar, V., Holt III, F. V., Collins Jr., E. G., and Alvi, F. S., “Microjet-based Separation Control Using a Virtual Sensor for Degree of Separation,” *Florida Center for Advanced Aero-Propulsion Annual Technical Symposium*, FCAAP, Tallahassee, Fl, Aug. 2009.
- <sup>9</sup>Kumar, V. and Alvi, F. S., “Towards Understanding and Optimizing Separation Control Using Microjets,” *AIAA*, Vol. 47, No. 11, Nov. 2009, pp. 2544–2557.
- <sup>10</sup>Favier, J., Kourta, A., and Leplat, G., “Control of Flow Separation of a Wing Profile using PIV Measurements and POD Analysis,” *IUTAM Symposium on Flow Control with MEMS*, IMFT - French National Institute of Mechanics of Toulouse, IUTAM, Sept. 2006.
- <sup>11</sup>Tian, Y., Song, Q., and Cattafesta, L., “Adaptive Feedback Control of Flow Separation,” *3rd AIAA Flow Control Conference*, Interdisciplinary Microsystems Group, AIAA, Reston, VA, June 2006.
- <sup>12</sup>Tian, Y. and Cattafesta, L., “Adaptive Control of Flow Separation,” *44th Aerospace Sciences Meeting and Exhibit*, Interdisciplinary Microsystems Group, AIAA, Reston, Va, Jan. 2006.
- <sup>13</sup>Alvi, F. S., “Adaptive Control of Inlet Separation Using Supersonic Microjets,” Tech. rep., NASA Langley Research Center, Hampton, VA.
- <sup>14</sup>Kumar, V. and Alvi, F. S., “Efficient Control of Separation Using Microjets,” June 2005.
- <sup>15</sup>Dunlap, D. D., Caldwell, C. V., and Jr., E. G. C., “Nonlinear Model Predictive Control Using Sampling and Goal-Directed Optimization,” *Mechanical Engineering*, Vol. 16, 2010, pp. 1349–1356.
- <sup>16</sup>Dunlap, D., Yu, W., Collins, E. G., and Caldwell, C. V., “Motion Planning for Steep Hill Climbing,” *2011 IEEE International Conference on Robotics and Automation*, IEEE, 2011, pp. 707–714.
- <sup>17</sup>“Motion Planning for Mobile Robots Via Sampling-Based Model Predictive Optimization,” .
- <sup>18</sup>Kuffner, J. J. and LaValle, S. M., “RRT-connect: An efficient approach to single-query path planning,” *Proceedings 2000 ICRA Millennium Conference IEEE International Conference on Robotics and Automation Symposia Proceedings Cat No00CH37065*, Vol. 2, No. Icara, 2000, pp. 995–1001.
- <sup>19</sup>LaValle, S. M. and Kuffner, J. J., “Randomized Kinodynamic Planning,” *The International Journal of Robotics Research*, Vol. 20, No. 5, 2001, pp. 378–400.
- <sup>20</sup>Pengo, T., Muoz-Barrutia, A., and Ortiz-De-Solrzano, C., “Halton sampling for autofocus.” *Journal of Microscopy*, Vol. 235, No. 1, 2009, pp. 50–58.
- <sup>21</sup>Chi, H., Mascagni, M., and Warnock, T. T., “On the optimal Halton sequence,” *Mathematics and Computers in Simulation*, Vol. 70, No. 1, 2005, pp. 9–21.
- <sup>22</sup>Rowley, C., Colonius, T., and Murray, R., “Model Reduction for Compressible Flows Using POD and Galerkin Projection,” *Physica D: Nonlinear Phenomena*, Vol. 189, No. 1, 2004, pp. 115–129.
- <sup>23</sup>Kim, K., Beskok, A., and Jayasuriya, S., “Nonlinear system identification for the interaction of synthetic jets with a boundary layer,” *American Control Conference, 2005. Proceedings of the 2005*, June 2005, pp. 1313 – 1318 vol. 2.
- <sup>24</sup>Platt, J., “A Resource-Allocating Network for Function Interpolation,” *Neural Computation*, Vol. 3, No. 2, 1991, pp. 213–225.
- <sup>25</sup>Yingwei, L. Y. L., Sundararajan, N., and Saratchandran, P., “Performance evaluation of a sequential minimal radial basis function (RBF) neural network learning algorithm.” *IEEE Transactions on Neural Networks*, Vol. 9, No. 2, 1998, pp. 308–318.
- <sup>26</sup>“A sequential learning scheme for function approximation using minimal radial basis function neural networks.” *Neural computation*, Vol. 9, No. 2, 1997, pp. 461–478.